AIMS Materials Science, 12(6): 1126–1152.
DOI: 10.3934/matersci.2025053
Received: 05 September 2025
Revised: 01 November 2025
Accepted: 12 November 2025
Published: 27 November 2025

https://www.aimspress.com/journal/Materials

Research article

High-performance lead-reduced bismuth-based alloys: Structural, mechanical, and radiation shielding synergy via rapid quenching

Mohamed Saad[1], Nadiah Almohiy[2], Hussain Almohiy[1], Abdelmoneim Saleh[3,4] and Rizk Shalaby[5]

[1] Department of Radiological Sciences, College of Applied Medical Sciences, King Khalid University, Abha 61421, Saudi Arabia
[2] Diagnostic Radiology, Medical Imaging, Ministry of National Guard Health Affairs, Riyadh, Saudi Arabia
[3] Basic Science Department, Higher Technological Institute, 10th of Ramadan City, 228, Egypt
[4] Faculty of Health Sciences, Universiti Sultan Zainal Abidin (UniSZA), 21300 Kuala Nerus, Terengganu, Malaysia
[5] Applied Materials and Metal Physics Research Laboratory, Physics department, Faculty of Science, Mansoura University, Mansoura, Egypt

* **Correspondence**: Email: rizk2002@mans.edu.eg; Tel: +2-010-6250-7736.

Abstract: This study investigated the structural, mechanical, and ionizing-radiation shielding properties of Bi-based binary and ternary alloys (Bi–Pb–Sn) synthesized via rapid quenching using a melt-spinning technique. X-ray diffraction (XRD) analysis revealed crystalline phase formation with reduced grain sizes, while scanning electron microscopy (SEM) images confirmed homogeneity in the microstructure. Mechanical testing showed that the Bi-5Pb35Sn alloy achieved the highest microhardness of 50.4 H_V, tensile strength of 126 MPa, and Young's modulus of 20.8 GPa, indicating enhanced resistance to premature fracture. Radiation shielding characteristics were evaluated using both MCNP5 simulation and WinXCOM software across photon energies of 0.015–15 MeV. The mass attenuation coefficient (μ/ρ) of the optimized alloy reached 1.22 cm^2/g at 0.06 MeV, with a corresponding half-value layer (HVL) of 0.56 cm, and radiation protection efficiency (RPE) exceeding 94.8%. The effective atomic number (Z_{eff}) ranged from 44.7 to 61.2 depending on photon energy, and relative deviation between MCNP5 and XCOM results remained below 4%, confirming the model's accuracy. Furthermore, the Bi-40Pb alloy also had superior neutron shielding properties (0.109 cm^{-1}) in comparison to typical neutron protecting materials, but Bi-50Sn had a

comparatively higher $\sum_R$ value. The incorporation of Sn significantly enhanced both mechanical integrity and shielding performance. These findings position the Bi40Pb10Sn50 alloy as a promising lead-reduced material with superior radiological and mechanical characteristics. Its performance supports its potential for practical applications in medical diagnostics, nuclear facility shielding, and radiation-safe industrial design, aligning with the need for efficient, non-toxic, and regulation-compliant shielding materials.

Keywords: mechanical characteristics; Bi-based alloys; MCNP; radiation protection; microstructure; microhardness

1. Introduction

Radioactive isotopes and nuclear radiation have recently been shown to have numerous scientific and technological applications, including nuclear medicine, radiotherapy, scientific research, agriculture, food irradiation, industry, communications, nuclear power plants, elemental analysis, space technology applications, irradiation response test, void and defect checks for materials used in industrial and medical settings, thermal neutron therapy, and neutron diffraction [1–3]. However, gamma and neutron radiation harm human cells, animals, and the environment. To avoid such adverse impacts, many researchers are interested in discovering the optimal radiation shielding qualities for various types of materials in radiation applications [4–6]. Any material may be used as radiation shielding provided it has sufficient thickness to withstand radiation to a reasonable degree. The absorption and dispersion of gamma rays are defined in terms of atomic number and density of an element; in mixtures, it is related to Z_{eff} and density. In this context, materials, such as glasses [7–9], ferrites [10], and nanocomposites [11], are considered as appropriate options for shielding against radiation.

Metallic alloys hold significant potential for industrial use due to their unique chemical, mechanical, and magnetic properties. These materials have garnered considerable interest as alternatives to traditional materials and are widely utilized across diverse fields such as transportation, aerospace, biomedical engineering, modern technology, pharmaceuticals, and radiation shielding. Their key advantage lies in being composed of two or more elements with differing structures, which can enhance properties like corrosion resistance, hardness, and tensile strength compared to the individual base elements [12].

From an environmental standpoint, Bi-based alloys present a significantly safer alternative to conventional Pb-based shielding materials. Bismuth is considered one of the least toxic heavy metals and is not classified as a hazardous substance under the European RoHS directive. This makes Bi-based alloys inherently more environmentally friendly in terms of production, handling, and end-of-life disposal. Moreover, bismuth's low solubility in biological systems reduces the risks of bioaccumulation and environmental contamination [13,14]. These attributes support the growing trend toward the adoption of sustainable and non-toxic shielding materials in the medical and nuclear fields. While the use of Pb in small concentrations (as in the ternary Bi–Sn–Pb systems) may still raise regulatory concerns, efforts to reduce or replace Pb with Sn or other non-toxic elements are under ongoing investigation to further enhance the eco-compatibility of these alloys [15,16]. Recent advances in the development of bismuth-based materials have demonstrated their promising potential as

effective shielding systems. Bismuth's high atomic number, low toxicity, and favorable mechanical properties have encouraged its incorporation into a range of alloys and composites tailored for radiation protection. For instance, Bi–Sn–Pb and Bi–Sn–Zn alloys have shown significant attenuation performance along with enhanced ductility and corrosion resistance, making them suitable for flexible shielding configurations in nuclear and medical applications [17,18]. Moreover, bismuth has been successfully integrated into polymeric and glass matrices, where its high photon interaction cross-section contributes to improved gamma-ray shielding capabilities without compromising environmental safety [19,20]. In nanostructured forms and composite matrices, Bi-based systems have also been optimized for multifunctional roles, combining electromagnetic interference shielding with radiation attenuation [21,22]. Additionally, microstructural control in bismuth oxide and bismuth–metal composites has enabled tunable mechanical and shielding performance, revealing their versatility across diverse radiation energy ranges [23]. These advances collectively underscore the importance of continued innovation in Bi-containing systems, and the present study aims to build upon this foundation by systematically optimizing the mechanical and shielding characteristics of rapidly quenched Bi–Sn–Pb alloys, addressing both structural integrity and radiation protection efficacy. The physical properties and neutron and gamma–ray shielding features of different metallic-based alloys, in applications such as gamma-ray shielding materials (e.g., tin-based systems), have been reported [24,25]. Bi-based binary and ternary alloys have gotten the most attention in mechanical and radiation shielding, as they present a number of benefits, including ease of manufacturing, high density, similarity to lead-based alloys, high joint strength, strong creep resistance, superior wettability, convenient mechanical and thermo-physical properties, relatively low cost, and high corrosion resistance. In this context, Bi–Pb–Sn alloys offer a promising combination of shielding efficiency and material safety, which supports their consideration for practical applications, particularly in medical and nuclear fields [26,27]. As a result, in this work, we propose to create and synthesize innovative high-performance metallic alloys for radiation shielding applications. We choose different series depending on Bi and varied Sn chemical compositions. The three elements mentioned above, Bi, Pb, and Sn, have distinct applications, such as solder application in electronics packaging and assemblies due to low melting points, bearing alloys, and brazing because of several advantages such as abundance, low cost, ease of production, low melting points, high strength, creep resistance, thermal stability, corrosion resistance, and wettability. In this work, "lead-reduced" refers to ternary Bi–Pb–Sn formulations (S2–S5) with substantially lower Pb fractions than pure Pb or typical Pb–Sb alloys; S1 (Bi-40Pb) is included as a high-Pb reference benchmark to quantify shielding/mechanical trade-offs.

The objective of this study is to investigate the balance between the structure, mechanical, and nuclear radiation (X/gamma rays, fast neutrons, and charged ions) shielding features of a new series of Bi–Pb, Bi–Pb–Sn, and Bi–Sn-based alloys for high-performance shielding materials in medical and nuclear applications using the MCNP code and the XCOM program. The following procedures were carried out to achieve this objective:

1. The melt-spun technique arrangement was used to fabricate the current alloys.

2. The structural and morphological properties of the fabricated alloys were analyzed using X-ray diffraction (XRD) and scanning electron microscopy (SEM) methods.

3. The density of the prepared alloys was measured experimentally.

4. Various effective parameters of X/gamma rays protection were estimated using the MCNP code and the XCOM program in a wide energy range.

5. The effective removal cross-section (Σ_R) for fast neutrons was determined and compared to standard neutron shielding materials.

6. Mass stopping powers (MSP) and projected ranges (PR) for protons and alpha particles were evaluated across an energy range of 0.01–15 MeV.

2. Materials and methods

2.1. Synthesis of Bi-based binary and ternary metallic alloys

Three types of shielding alloys were synthesized using high-purity metals (Bi (99.98%), Pb (99.96%), and Sn (99.99%)): Bi-40Pb, Bi-30Pb-10Sn, Bi-20Pb-20Sn, Bi-10Pb-30Sn, Bi-5Pb-35Sn, and Bi-50Sn, purchased from Prolabo, France. To obtain the fabricated shielding alloys in the final form, the experiment was carried out in two stages. First, the alloys with the above nominal compositions were placed in a graphite crucible and melted in an electric furnace at approximately 450 °C (Figure 1a). Then, the molten alloys were thoroughly stirred to ensure homogeneity and returned to the furnace for an additional 10 min (or less) to complete mixing. The molten alloys were cooled to room temperature in a thermal glass tube (cylindrical shape, diameter 10 mm). The cylinder alloys were cut into small pieces (diameter 10 mm, thickness 5 mm) and placed in the simple single-roller melt-spinning technique, as schematically illustrated in Figure 1b. This figure shows alloy melting, ejection through a nozzle, rapid solidification on the rotating copper wheel, and final formation of ribbon samples. The molten alloy was ejected through a small orifice onto the surface of a copper wheel rotating at 30 m/s, producing long ribbons in air. This simple and easy method facilitates the subsequent mechanical testing and characterization. The solidification rate was estimated from $R = tv/d$, where R is the solidification rate, t is the ribbon thickness, v is the wheel velocity, and d is the distance between the orifice and the copper wheel.

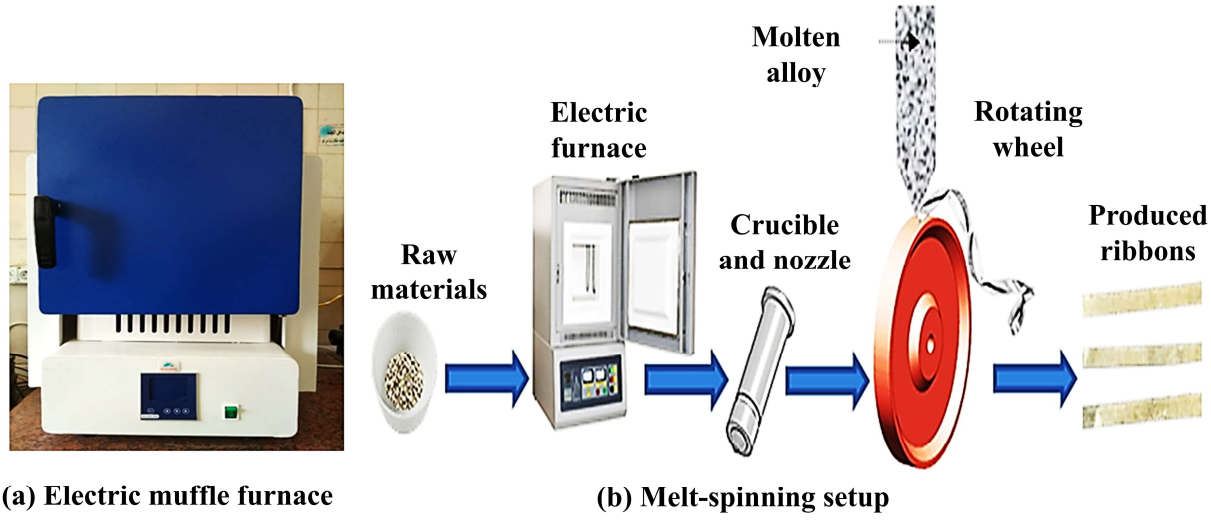

Figure 1. (a) Electric muffle furnace. (b) Schematic diagram of the melt-spinning setup.

The chemical concentrations and experimental and theoretically evaluated densities of the shielding alloys are presented in Table 1. The densities of synthesis samples (ρ) were calculated using Archimedes' principle equation (Eq 1):

$$\rho = \frac{W_a}{W_a - W_b} \times \rho_{dw} \quad (1)$$

where W_a and W_b are the weights of the alloy sample in the air and water, respectively, and W_{dw} is the density of the distilled water. Five repeated density measurements were made for each alloy. Photos of all alloy types are shown in Figure 2. The theoretical densities of the fabricated alloys were calculated using the rule of mixtures based on the elemental composition and standard atomic densities. The results show both experimental and calculated densities, along with percentage deviations. The minor discrepancies are attributed to micro-voids and minor porosity.

Table 1. Chemical concentrations (wt.%), sample codes, and experimental and theoretical densities of fabricated Bi-based alloys.

Shielding alloy	Sample code	Chemical composition (wt.%)			Experimental density (g/cm^3)	Theoretical density (g/cm^3)
		Bi	Pb	Sn		
Bi-40Pb	S1	60	40	-	10.39 ± 3.84	10.416
Bi-30Pb-10Sn	S2	60	30	10	9.99 ± 4.28	10.011
Bi-20Pb-20Sn	S3	60	20	20	9.58 ± 2.38	9.606
Bi-10Pb-30Sn	S4	60	10	30	9.18 ± 5.26	9.201
Bi-5Pb-35Sn	S5	60	5	35	8.98 ± 2.57	8.9985
Bi-50Sn	S6	50	-	50	8.53 ± 4.21	8.545

Figure 2. Suitable shape of synthesis shielding alloys using the melt-spun process.

2.2. Mechanical characteristics of Bi-based alloys

In the current study, two techniques were used to characterize the mechanical features of the shielding alloys. First, the mechanical characteristics and elastic moduli of the synthesized Bi-based metallic alloys were evaluated using a tensile test machine [27,28]. Samples with dimensions

of 40 × 4 × 2 mm were tested at a tensile rate of 0.5 mm/min to obtain a typical stress–strain curve. Second, the Vickers microhardness (H_V) was determined using a Vickers microhardness tester (Model FM 7, Tech Group Tokyo, Japan), equipped with a diamond indenter. Tests were conducted under different loads ranging from 0.098 to 1.96 N until sample fracture or deformation, with indentation durations from 1 to 10 min. For each specimen, 15 consecutive values were obtained with approximately 40 μm between each indent mark; the mean value was considered as the microhardness value. The lowest and highest H_V values were ignored, and the remaining nine values were used, as well as the standard deviation. Before microhardness testing, sample surfaces were carefully ground using progressively finer silicon carbide papers (400–2000 grit), followed by polishing with 1 μm diamond paste to achieve a mirror-like finish. The polished surfaces were then cleaned with ethanol and dried with warm air to eliminate any contaminants or residues that could affect indentation accuracy.

2.3. Structural characterization of Bi-based alloys

The phase identification and crystal structure of the synthesized metallic alloys were examined using XRD with an X-ray diffractometer (PANalytical, radiation source CuKα = 1.54056 Å). The specimens were directly scanned at 2θ angles between 20 and 100°. Surface morphology and microstructure of the alloys were investigated using scanning electron microscopy (SEM; JSM-6510 LV JEOL, Japan), working at 30 kV with high resolution in high vacuum mode, with a spatial resolution of 3.0 nm. Shielding alloys were mechanically polished and cleaned before the microscopic tests. Each sample was electrochemically etched in a solution of 10% nitric acid (HNO_3), 10% hydrochloric acid (HCl), and 80% ethyl alcohol (C_2H_5OH). Crystallite sizes were estimated using the Debye–Scherrer formula, assuming that line broadening arises primarily from finite crystallite dimensions. No instrumental standard was used to correct for instrumental broadening; thus, the reported values should be considered approximate and are primarily used for comparative purposes across the alloy series. The SEM images revealed contrast variations attributed to different phases and microstructural features formed during the rapid solidification process. While the distribution appeared uniform and without agglomeration, we note that no elemental mapping or energy-dispersive X-ray spectroscopy (EDX) analysis was performed to confirm the chemical composition of the observed phases. Therefore, the conclusions regarding phase distribution are qualitative and primarily supported by the XRD analysis. Furthermore, although the samples were etched to improve topographic contrast, we acknowledge that etching may potentially obscure or alter the visibility of some phases.

2.4. Ionized radiation shielding estimation

2.4.1. The MCNP simulation method

Radiation shielding simulations were carried out using the Monte Carlo N-Particle Transport Code (MCNP5) to evaluate the gamma-ray attenuation behavior of the synthesized Bi-based alloys. A monoenergetic, point isotropic gamma-ray source was defined, with energies ranging from 0.015 to 15 MeV, consistent with the photon energy range used in WinXCOM calculations. The gamma-ray source was positioned at a fixed distance of 2.0 cm from the front face of the alloy sample to simulate realistic irradiation geometry. The sample was modeled as a cylindrical slab with a diameter of 2 cm

and varying thicknesses to assess shielding efficiency and attenuation behavior. Air was defined as the surrounding medium. The simulation geometry was constructed using surface cards to define a cylindrical cell filled with the alloy composition derived from experimental mass fractions. Material definitions were input using the M card, and elemental compositions matched the experimental alloy formulations. Photon transport physics (mode P) was activated, and ENDF/B-VII cross-section libraries were used for accurate gamma interaction data. The photon flux tally (F4:P) was employed to measure the average photon flux in a defined detector region behind the sample. These were used to derive the linear attenuation coefficient (μ) and calculate the mass attenuation coefficient (μ/ρ) by normalizing with the alloy density. The dose rate behind the shield was also determined using F6 tallies and converted to dose equivalents using fluence-to-dose conversion factors. To ensure statistical reliability, each simulation was run with 10^8 particle histories. The relative errors in the tally results were maintained below 2% for all photon energies, ensuring high confidence in the derived shielding parameters. Simulation outputs were validated by comparing the μ/ρ values obtained from MCNP5 with those calculated using WinXCOM. The relative deviation between both methods was found to be below 4%, confirming the validity and consistency of the MCNP5 modeling approach for evaluating gamma shielding behavior. The 3D model of the present study is illustrated in Figure 3 [29,30].

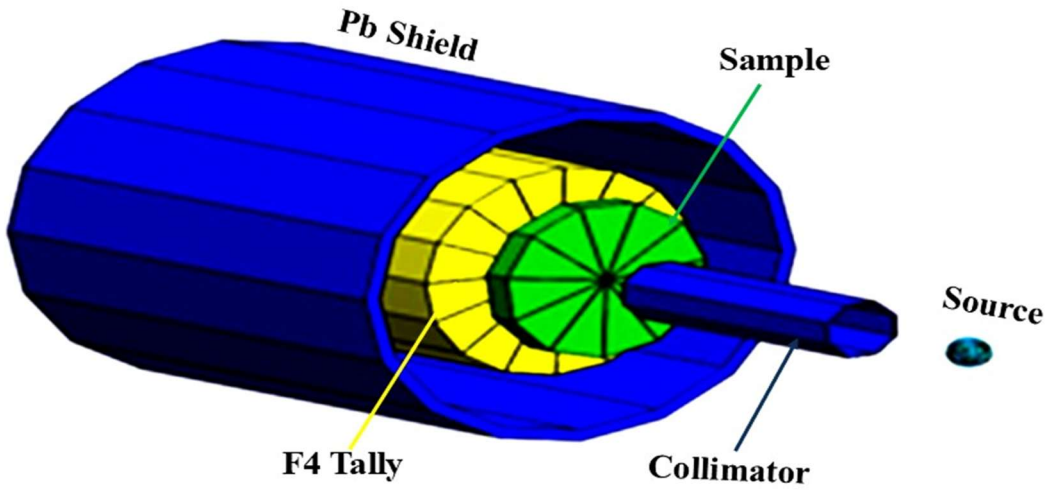

Figure 3. The MCNP 3D Visual Editor's model for estimating the gamma-ray mass attenuation coefficient values.

To evaluate the difference between the mass attenuation coefficient (μ/ρ) values obtained from the MCNP5 simulation and those computed via the XCOM software, the relative deviation (RD) was determined using Eq 2 [29]:

$$RD(\%) = \left|\frac{(\mu/\rho)MCNP \quad (\mu/\rho)XCOM}{(\mu/\rho)MCNPX}\right| \times 100\% \tag{2}$$

This formula expresses the relative deviation as a percentage, quantifying the absolute difference between the MCNP5 and XCOM results, normalized against the MCNP5 output.

The photon shielding capabilities of the investigated Bi-based alloys were examined by calculating the mass attenuation coefficient (μ_m), which indicates a material's capacity to attenuate

gamma photons of varying energies (Eq 3). These values were obtained using the WINXCOM software, applying the mixture rule across a photon energy range of 0.015–15 MeV [30]:

$$\mu_m = \sum_i w_i \left(\frac{\mu}{\rho}\right)_i \tag{3}$$

where w_i is the weight fraction, and $(\mu/\rho)_i$ is the mass attenuation coefficient of the i^{th} element in the alloy.

The half-value layer (HVL), a key parameter in characterizing gamma radiation shielding performance, represents the material thickness required to reduce the incident photon intensity by half. It is energy-dependent and provides insight into the penetration ability of gamma photons. HVL was calculated using Eq 4 [31]:

$$HVL = \frac{\ln(2)}{\mu} \tag{4}$$

where μ is the linear attenuation coefficient in cm^{-1}.

Additional shielding parameters, including the total atomic cross-section (σ_a), electronic cross-section (σ_e), effective atomic number (Z_{eff}), and electron density (N_{el}), were also derived from the μ_m values.

The total atomic cross-section (σ_a) in cm^2/atom is calculated as Eq 5 [30]:

$$\sigma_{t,a} = \frac{\mu_m \sum_i n_i A_i}{N_A \sum_i n_i} \tag{5}$$

where w_i is the weight fraction, A_i is the atomic weight of element i, M is the molar mass of the alloy, and N_A is Avogadro's number.

Similarly, the total electronic cross-section (σ_e) in barns/atom is obtained by Eq 6 [30]:

$$\sigma_{t,el} = \frac{1}{N_A} \sum_i \frac{f_i A_i (\mu_m)_i}{Z_i} \tag{6}$$

To compute Z_{eff}, which reflects the average atomic number for a compound or alloy in terms of radiation interaction, the fraction $fi = n_i/\Sigma n_i$ (where Z_i is the atomic number of element i) is used. Z_{eff} is then derived using Eq 7:

$$Z_{eff} = \frac{\sigma_{t,a}}{\sigma_{t,el}} = \frac{\sum_i n_i A_i (\mu/\rho)_i}{\sum_i n_i A_i / Z_i (\mu/\rho)_i} \tag{7}$$

The electron density (N_{el}), indicating the number of electrons per gram of the alloy, can be obtained by Eq 8 [29]:

$$N_{el} = \frac{\mu_m}{\sigma_e} = \frac{Z_{eff} N_A \sum_i n_i}{M} \tag{8}$$

where Z_i is the atomic number, and M is the molar mass of the alloy.

Finally, the radiation protection efficiency (RPE), which reflects the effectiveness of the material in attenuating photon flux, was calculated using Eq 9 [29]:

$$RP\ (\%) = \left(1 - \frac{I}{I_0}\right) \times 100\% \quad (9)$$

where I_0 and I are the incident and transmitted gamma photon intensities, respectively.

2.4.2. Neutron attenuation characteristics

The neutron attenuation can be estimated in terms of the macroscopic effective fast neutron removal cross-section (Σ_R). Σ_R is a crucial parameter for evaluating the fast neutron attenuation capacity of materials used in shielding applications. It is approximately constant for neutron energies between 2 and 12 MeV and can be estimated using the mixture rule. The formula for calculating Σ_R is $\Sigma_R = \sum w_i(\Sigma_R/\rho)_i$ [31], where Σ_R is the macroscopic effective removal cross-section (cm^{-1}), and w_i is the partial density (g/cm^3) of the i^{th} constituent element. There are two main methods for determining Σ_R: calculation based on tabulated data and Monte Carlo simulation using the MCNP code. The accuracy of Σ_R values calculated using the mixture rule depends on the accuracy of the tabulated mass removal cross-sections. Low-Z elements, particularly hydrogen, generally increase Σ_R, but density also influences it. Σ_R is useful for designing effective neutron shielding materials, predicting neutron attenuation, and comparing the effectiveness of different materials in attenuating fast neutrons. Understanding the concept and its calculation methods is essential for developing and evaluating neutron shielding materials [31,32].

3. Results and discussion

3.1. XRD structural analysis for Bi-based shielding alloys

XRD provides the most definitive information about phase identifications, lattice parameters, and structural data. The XRD analysis of the nominal alloys Bi-40Pb, Bi-30Pb-10Sn, Bi-20Pb-20Sn, Bi-10Pb-30Sn, Bi-5Pb-35Sn, and Bi-50Sn is depicted in Figure 4. The XRD patterns of Bi-40Pb (Figure 4a) contain a rhombohedral hexagonal pattern (PDF 01-085-5853) with space group R-3m (166), as well as a hexagonal Bi0.3Pb0.7 solid solution phase formed by partial substitution between Bi and Pb atoms (pattern no. PDF 01-072-5625) with space group P63/mmc (194). After adding 10 wt.% Sn, the presence of a tetragonal bismuth-tin phase (Sn0.95Bi0.05, pattern no. PDF 01-074-5514) is observed along with rhombohedral H.axes α-Bi (pattern no. PDF 00-044-1246 S.G. R-3m (166), as shown in Figure 4b. This suggests that Sn is soluble within the Bi–Pb matrix, forming a solid solution with bismuth, identified as Sn0.95Bi0.05, rather than a distinct intermetallic compound.

At 20 wt.% Sn addition, both α-Bi and intermetallic compounds (IMCs) Sn0.95Bi0.05 and Bi0.3Pb0.7 appear, as shown in Figure 4c. Figure 4d,e shows the presence of two different tetragonal β-Sn phases—one with S.G. I41/amd (141) and pattern no. PDF 01-085-5859, and another with pattern no. PDF 01-085-5858—along with IMC Bi0.3Pb0.7 and α-Bi.

As shown in Figure 4f, the XRD pattern indicates the presence of two IMCs, Bi0.3Pb0.7 and Sn0.95Bi0.05, as well as α-Bi. On the other hand, for the Pb-free alloy, only two phases, tetragonal β-Sn and rhombohedral α-Bi, are observed, with no IMC present.

The detailed XRD results and the lattice parameters of different distinct phases are summarized in Table 2. The lattice parameters of each phase were calculated from the experimental XRD data using

Bragg's law and the appropriate unit cell geometry equations. The results are presented in Table 2. These values show a trend corresponding to the gradual substitution of Pb with Sn, where the lattice parameters of intermetallic compounds such as Bi0.3Pb0.7 and Sn0.95Bi0.05 exhibit slight shifts, consistent with the incorporation of smaller Sn atoms in place of larger Pb or Bi atoms. This lattice contraction confirms successful alloying and substitution effects in the melt-spun samples.

The average crystallite size (D) of shielding alloys was calculated using Debye-Scherrer's equation, as Eq 10 [24]:

$$D = \frac{k\lambda}{\beta cos\theta} \tag{10}$$

where $k = 1$, $\lambda = 1.54056$ Å for CuKα, β is the full width at half maximum (FWHM) in radians, and θ is the Bragg angle [24,25].

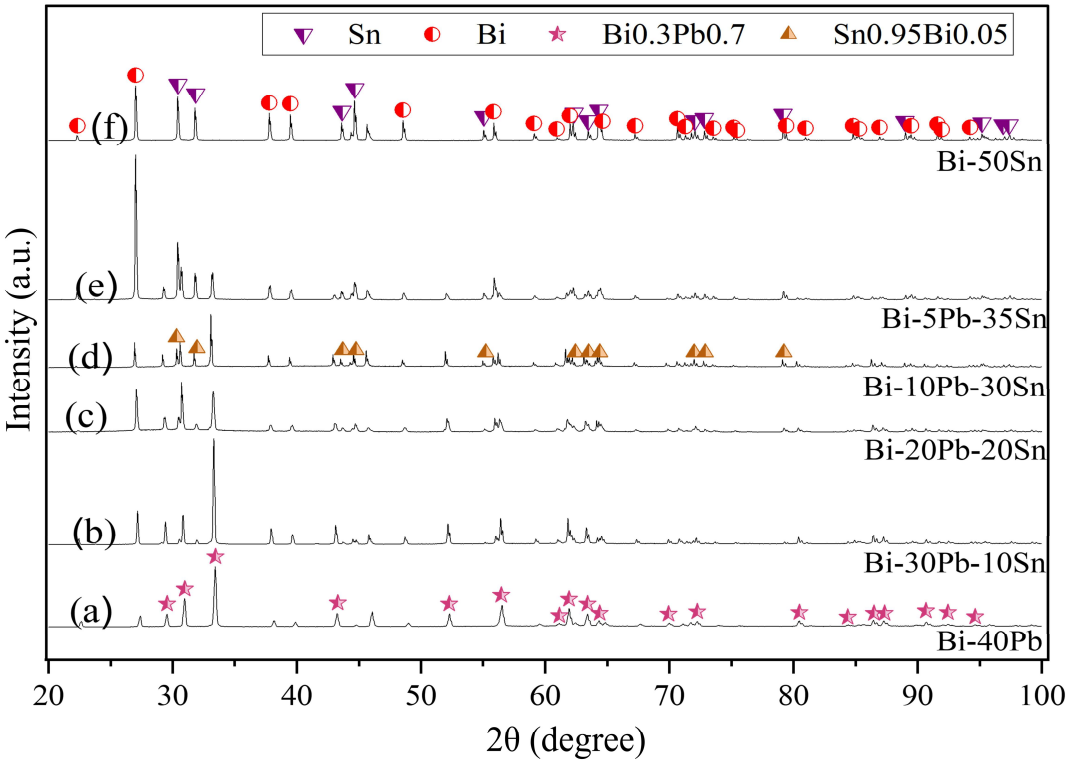

Figure 4. X-ray diffraction pattern for binary and ternary Bi-based metallic alloys.

Table 2. XRD details of the prepared Bi–Pb–Sn alloys.

Shielding alloy	Card No.	Phase designation	Crystal system	Lattice constants (Å)		Crystallite size D (nm) Scherrer	No. of atoms/unit cell of Sn phase	Strain (ε, %)
				a	c			
Bi-40Pb	PDF 01-085-5853	Bi	Rhombo.H.axes	4.545	11.900	393.23	4.25	0.00171
	PDF 01-072-5625	Bi0.3Pb0.7	Hexagonal	3.505	5.79			
Bi-30Pb-10Sn	PDF 01-072-5625	Bi0.3Pb0.7	Hexagonal	3.505	5.79	350.25	4.21	0.00154
	PDF 00-044-1246	Bi	Rhombo.H.axes	4.545	11.900			
	PDF 01-074-5514	Sn0.95Bi0.05	Tetragonal	5.857	3.190			
Bi-20Pb-20Sn	PDF 01-072-5625	Bi0.3Pb0.7	Hexagonal	3.505	5.79	355.23	4.05	0.00133
	PDF 01-085-5857	Bi	Rhombo.H.axes	4.545	11.900			
	PDF 01-074-5514	Sn0.95Bi0.05	Tetragonal	5.857	3.190			
Bi-10Pb-30Sn	PDF 01-085-5858	Sn	Tetragonal	5.881	3.202	320.45	4.01	0.00124
	PDF 01-072-5625	Bi0.3Pb0.7	Hexagonal	3.505	5.79			
	PDF 01-085-5857	Bi	Rhombo.H.axes	4.545	11.900			
	PDF 01-085-5859	Sn	Tetragonal	5.881	3.202			
Bi-5Pb-35Sn	PDF 01-085-5857	Bi	Rhombo.H.axes	4.545	11.900	291.36	3.97	0.00122
	PDF 01-074-5514	Sn0.95Bi0.05	Tetragonal	5.857	3.190			
	PDF 01-072-5625	Bi0.3Pb0.7	Hexagonal	3.505	5.79			
Bi-50Sn	PDF 01-085-5862	Sn	Tetragonal	5.860	3.193	280.23	3.96	0.00115
	PDF 01-085-5857	Bi	Rhombo.H.axes	4.545	11.900			

3.2. Morphology details using SEM of Bi-based shielding alloys

The phase distributions of the synthesized Bi–Pb–Sn metallic materials were examined using SEM, as depicted in Figure 5. Figure 5 illustrate the presence of eutectic Bi–Pb. Within the grains and at the grain boundaries, precipitates of IMCs are distributed and dispersed throughout the matrix. Figure 5 also shows a reduction in the grain size of the Bi and Sn phases with increasing Sn content. Additionally, all phases are uniformly distributed in the matrix without any segregation or agglomeration. This leads to the formation of a uniform microstructure inside the sample, minimizing microscopic defects. The irregular and equiaxed grains from the different phases are alternately distributed along the X–Y and X–Z planes of the sample.

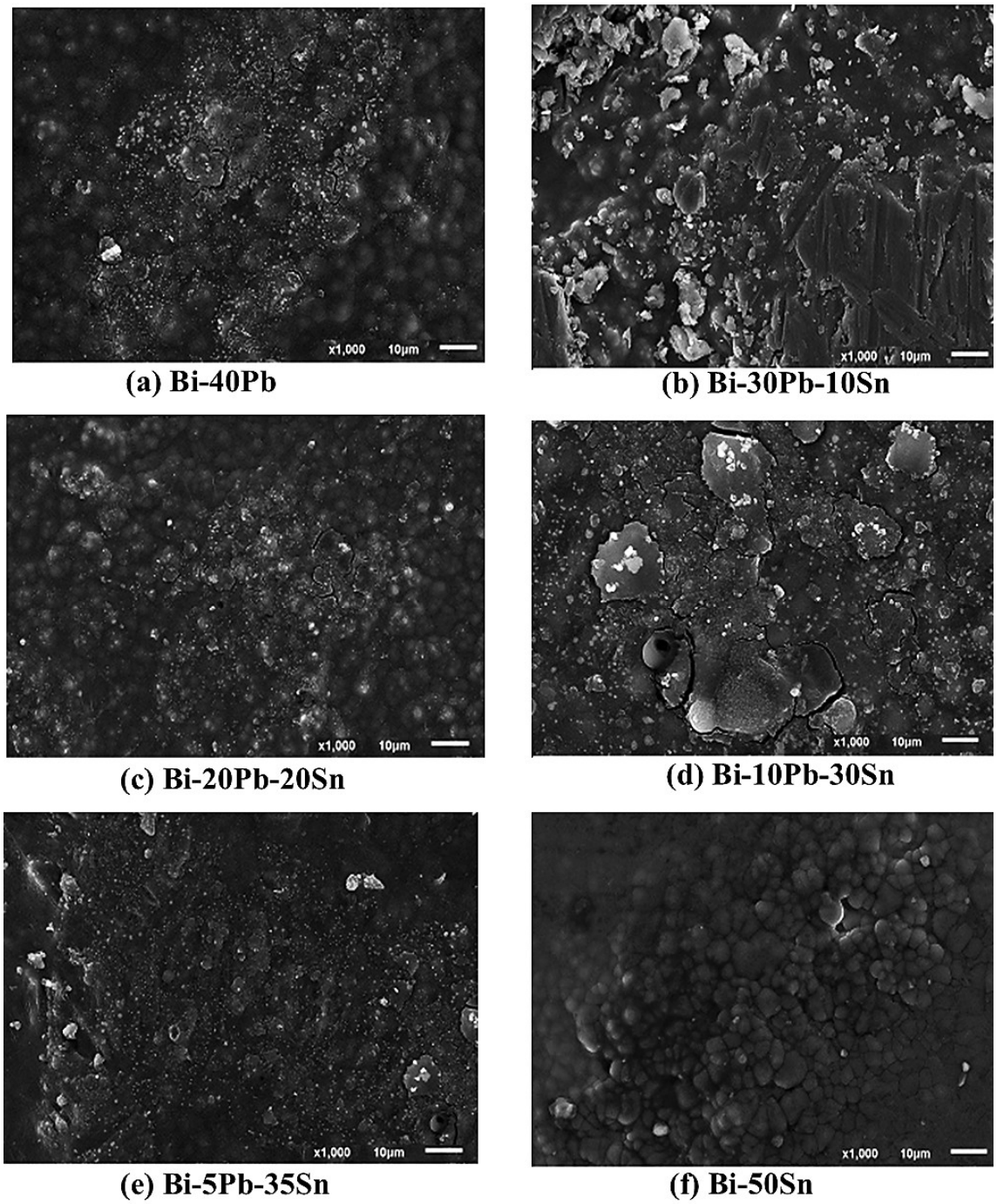

Figure 5. Microstructure characteristics using scanning electron microscopy of as-prepared materials.

It can be concluded that the grain size is significantly refined at high Sn concentrations, which may be attributed to the low melting point of Sn (approximately 230 °C), and the extended solubility range caused by the rapid quenching process. In general, the grain size (d) can be expressed as Eq 11 [24]:

$$d = a(Rc)^{-1} \tag{11}$$

where *Rc* is the cooling rate, and a and n are the coefficients related to materials. The above equation proves that the grain coarsening in Bi–Pb–Sn samples is indeed caused by the cooling rate *Rc* in the melt-spun process: the smaller the *Rc*, the larger the grain diameter *d*. It is also well known that reducing or decreasing the microstructural scale enhances and optimizes the mechanical stiffness of materials. The microstructural analysis confirms that the Bi–Pb-rich matrix (darker regions) and some IMCs (lighter regions) exhibit a typical agglomerated or flower-like regular eutectic morphology.

The microstructure, as revealed by SEM, plays a critical role in defining the mechanical performance of the alloys. The uniform distribution of fine phases within the Bi-rich matrix—particularly after Sn addition—leads to grain refinement, which increases the total grain boundary area. Grain boundaries act as barriers to dislocation motion, thereby enhancing strength and hardness via the Hall–Petch mechanism. Additionally, the presence of solid solution phases (e.g., Bi0.3Pb0.7 and Sn0.95Bi0.05) introduces lattice distortions that further hinder dislocation movement, contributing to solid solution strengthening. The combination of eutectic structures, secondary phase dispersion, and refined grains supports the improved mechanical performance (e.g., higher microhardness, yield strength, and Young's modulus) observed in Sn-rich alloys such as Bi-5Pb-35Sn. Furthermore, the absence of phase agglomeration or porosity in the SEM images indicates good metallurgical bonding and microstructural integrity, which contributes to the alloys' enhanced ductility and toughness.

3.3. Vickers microhardness and tensile properties investigations

The Vickers microhardness test (H_V) is a convenient technique to investigate the mechanical properties of as-prepared samples. This method is convenient: relatively small pieces of test samples are needed, there are no strict requirements for the shape of the test specimen, and investigations can be carried out without destroying the specimen. Vickers microhardness measurements (H_V) of the as-prepared alloys were performed using a FM-7 model (Japan) digital microhardness tester at room temperature. Several low/high loads were applied: 10, 25, 50, 100, 200, 500, and 1000 gf, at a constant indentation time of 10 s. The measured values were estimated using the standard Vickers formula (Eq 12):

$$H_v = \frac{2P\sin\frac{\theta}{2}}{d^2} = \frac{1.8544(P)}{d^2} \tag{12}$$

Figure 6 shows the H_V microhardness values of Bi–Pb–Sn shielding alloys with different compositions. The maximum hardness is observed for the Bi-5Pb-35Sn, reaching 650.22 MPa, compared with 512 and 490 MPa for Bi–Pb and Bi–Sn, respectively. This suggests that the ternary Bi-5Pb-35Sn sample has superior microhardness. The low values for the binary alloys can be attributed to the presence of soft α and β solid-solution phases related to soft lead and tin elements. On the other hand, the highest value for the ternary Bi–Pb–Sn can be explained by the increased Sn content, which enhances microhardness at the grain boundaries of different phases. This improvement is primarily due to several strengthening mechanisms: (i) precipitation strengthening from Sn particles, which hinder dislocation movement according to the Orowan mechanism. (ii) Second-phase strengthening from the melt-spinning process, which effectively restricts dislocation mobility. The melt-spinning process induces rapid solidification, which leads to the formation of fine intermetallic compounds and second-phase particles such as Bi0.3Pb0.7 and Sn0.95Bi0.05 dispersed within the Bi-rich matrix. These hard, secondary phases act as obstacles to dislocation motion by creating internal stress fields

and phase boundaries. This impedes the glide of dislocations, thereby increasing the yield strength and hardness. The uniform dispersion and refined size of these second-phase particles contribute to a more effective pinning of dislocations, a mechanism commonly described as second-phase particle strengthening. (iii) Anisotropic microstructure effects in the Bi–Sn matrix. However, a reduction in hardness may occur due to grain coarsening, which decreases the number of grain boundaries in the indentation zone, lowers the hardening effect, and reduces dislocation density. This relationship is described by Eq 13 [24]:

$$H = H_0 - Kd^{-0.5} \tag{13}$$

where H is the microhardness, d is the grain diameter, and H_0 and K are constants. According to this expression, larger grain sizes result in lower hardness values.

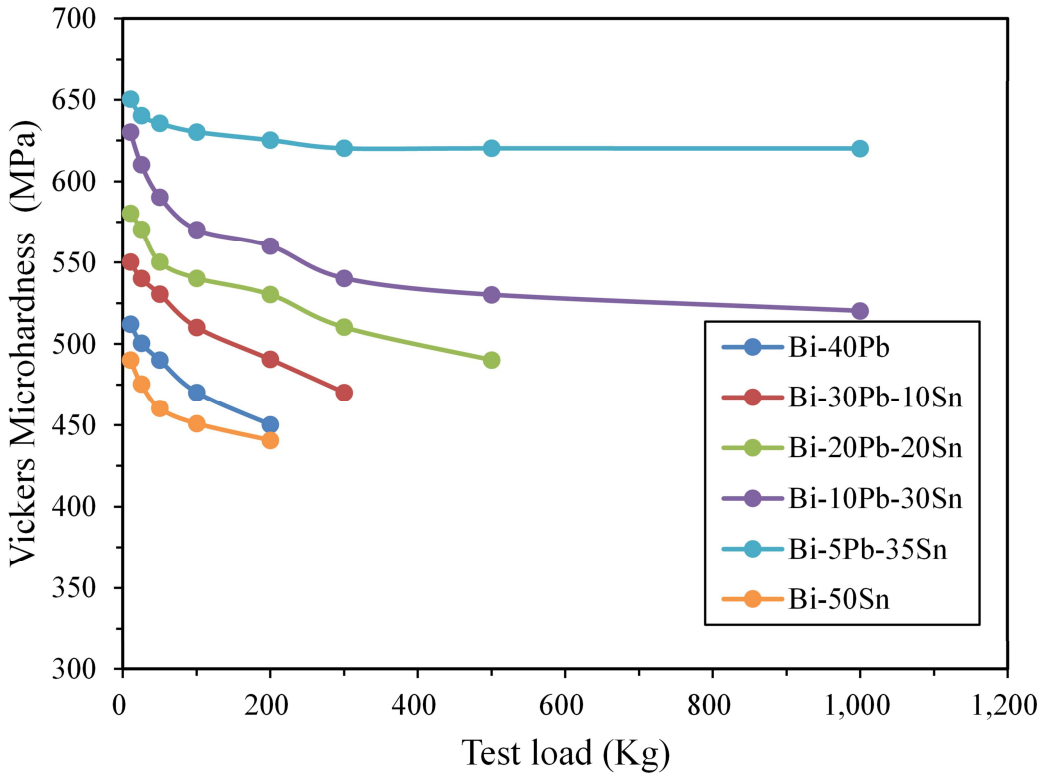

Figure 6. Vickers microhardness measurements (H_V) for Bi–Pb–Sn shielding alloys.

The tensile properties and elastic constants are essential indicators of the mechanical performance of the samples, which were evaluated using tensile testing machine, as briefly discussed in [25]. Figure 7 shows the engineering stress–strain curves of Bi–Pb–Sn shielding materials measured at room temperature (30 °C). The elastic modulus, yield strength, ultimate tensile strength, toughness, and elongation are summarized in Table 3. It is observed that the Bi-5Pb-35Sn sample exhibits the highest mechanical performance among all prepared alloys. The Young's modulus varies from 40 to 60 MPa, the ultimate tensile strength (UTS) varies from 14 to 45 MPa, and elongation or ductility varies from 0.263 to 7.4 MJ/m^3. At the same time, mechanical performance of Bi-5Pb-35Sn reached maximum values: Young's modulus was 60.97 GPa, UTS was 45 MPa, and elongation was 7.4%. The addition of Sn particles at high concentrations plays a crucial role in improving the mechanical

properties of materials. The significant enhancement in mechanical properties with increasing Sn content can be attributed to two primary factors: (1) the presence of a stable Bi–Sn matrix structure and uniform dispersion of Sn particles at grain boundaries, which impedes dislocation motion and promotes strain hardening, resulting in increased strength and ductility; and (2) Sn particles, which are tightly bonded and free of cracks, can deflect growing fractures, increasing energy absorption and further enhancing ductility [33,34].

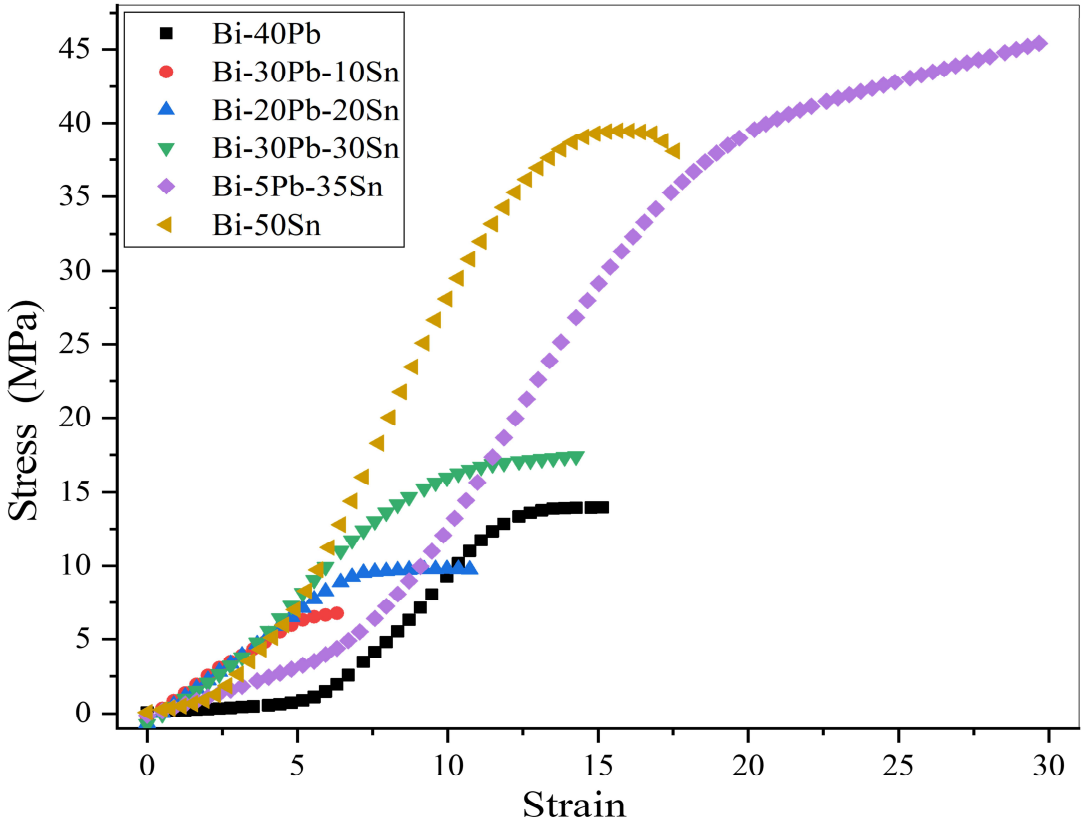

Figure 7. Stress–strain behavior curves for as-prepared Bi–Pb–Sn shielding materials after a melt-spun process.

Conversely, a decline in mechanical properties, particularly yield strength (YS), may occur due to grain coarsening. This leads to fewer grain boundaries, reduced dislocation resistance, and consequently lower yield strength. This effect is especially evident in the Bi–Sn sample and can be described by the Hall–Petch relationship (Eq 14):

$$\sigma_g = \sigma_0 + kd^{-0.5} \tag{14}$$

where σ_g is the yield strength, σ_0 is the yield strength of a single crystal, k is a material constant, and d is the average grain size [35]. According to Eq 14, as grain size increases, the material's strengthening effect diminishes. Interestingly, in the Bi–Sn alloy, the Sn-induced interfacial strengthening partially compensates for the negative impact of grain growth. Based on the observed microstructure and variations in UTS, the mechanical enhancement in Bi–Pb–Sn shielding alloys is primarily attributed to multiple strengthening mechanisms: solid solution strengthening, second-phase strengthening, grain refinement, and deformation strengthening. Prior to microhardness testing, SEM examination

confirmed that the alloy surfaces were free of visible micropores or cracks. The dense and uniform microstructure indicates that the influence of porosity on the hardness measurements is minimal. Additionally, the low standard deviations in H_V values support the reliability of the data.

Table 3. Mechanical characteristics for the as-prepared Bi–Pb–Sn materials after a melt-spun process.

Composition (wt.%)	Elastic modulus (GPa)	Ductility (%)	Yield stress (MPa)	UTS (MPa)	Fracture toughness (MPa $m^{1/2}$)
Bi-40Pb	45.75	3.880	5.00	14	05.33
Bi-30Pb-10Sn	43.18	1.263	6.50	7.5	07.25
Bi-20Pb-20Sn	49.99	1.690	8.50	10	09.44
Bi-10Pb-30Sn	54.98	3.548	15.0	17.5	12.56
Bi-5Pb-35Sn	60.97	7.446	35.00	43	15.36
Bi-50Sn	40.24	5.452	30.00	37	12.25

3.4. Shielding properties

The gamma-ray shielding characteristics were evaluated using the mass attenuation coefficient (μ/ρ). These μ/ρ values were calculated for the newly developed alloys across a radiation energy range of 0.01–15 MeV, utilizing both the XCOM software and the MCNP5 simulation code. Table 4 presents these values along with their relative deviations (RD%). Acquired data are shown in Figure 8 to fully comprehend how photon energy affects the μ/ρ values for the samples utilized in this investigation. Figure 8 suggests that there is a significant degree of correlation between the μ/ρ values of all manufactured samples obtained using the MCNP5 code and the XCOM values. Furthermore, Figure 8 shows the effect of incoming photon energy on μ_m values. Furthermore, an increase in the filler content of Sn results in decreased μ_m values. This is because the atomic number of Sn (Z = 30) is smaller than that of Pb (Z = 82). Partial photon interactions are responsible for the dependence of μ_m values on photon energy. In this context, the photoelectric effect (PE) is responsible for the rapid decrease of μ_m values in the low energy region (up to 0.15 MeV). Additionally, photoelectric absorption along the K and L edges of the bismuth element (Bi) produced the peaks observed in Figure 8. The dominance of Compton scattering (CS) interaction in energies between 0.05 and 5 MeV explains the little decrease in μ_m values. Such pair production interaction then causes μ_m values to progressively increase in the energies between 1.022 and 15 MeV. The Bi-40Pb alloy is considered the best sample for gamma-ray shielding among the alloys under investigation, as seen in Figure 8.

Table 4. The obtained mass attenuation coefficients (μ/ρ) using XCOM software and MCNP5 simulation code for the current alloys.

Energy (MeV)	S1			S2			S3		
	XCOM	MCNP5	RD (%)	XCOM	MCNP5	RD (%)	XCOM	MCNP5	RD (%)
0.015	114.24	115.6766	1.241878	107.74	112.013	3.814745	101.25	103.2057	1.894924
0.02	88.254	89.17514	1.03296	81.763	85.63623	4.522892	75.272	76.88909	2.103141
0.03	31.04	32.50304	4.501247	32.129	32.80512	2.061013	33.218	33.31403	0.28825
0.04	14.714	15.41971	4.576694	15.221	15.76064	3.423972	15.728	16.43305	4.290466
0.05	8.2436	8.511767	3.150546	8.5094	8.631943	1.419642	8.7752	8.822129	0.531945
0.06	5.1478	5.382394	4.358541	5.3023	5.482007	3.278132	5.4568	5.620716	2.916287
0.08	2.4808	2.601048	4.623075	2.5418	2.567561	1.003314	2.6028	2.620507	0.675707
0.1	5.6618	5.924544	4.434844	5.2746	5.345598	1.328159	4.8874	5.129849	4.726243
0.2	1.0192	1.050234	2.954946	0.95198	0.969877	1.84533	0.88472	0.901691	1.882146
0.3	0.41112	0.418101	1.669682	0.38719	0.394351	1.815982	0.36326	0.366111	0.778818
0.4	0.23638	0.238957	1.078277	0.22471	0.230674	2.585528	0.21304	0.214542	0.700018
0.5	0.16388	0.164399	0.315471	0.15712	0.160179	1.910013	0.15037	0.155416	3.246597
0.6	0.12654	0.129183	2.045598	0.12217	0.127234	3.979848	0.11781	0.118851	0.875652
0.8	0.089702	0.092618	3.148602	0.087494	0.089026	1.720335	0.085286	0.089261	4.452721
1	0.071692	0.074945	4.341031	0.07039	0.073857	4.694135	0.069088	0.072044	4.103081
2	0.046382	0.047131	1.589078	0.045887	0.046733	1.810475	0.045392	0.04739	4.216411
3	0.042616	0.043298	1.575328	0.042068	0.04325	2.733668	0.04152	0.042938	3.302181
4	0.042244	0.043788	3.526958	0.041607	0.043239	3.773646	0.04097	0.041496	1.266595
5	0.04299	0.04391	2.094242	0.042266	0.042905	1.489872	0.041542	0.043156	3.738861
6	0.044192	0.045288	2.420718	0.043384	0.044104	1.631635	0.042576	0.044677	4.702702
8	0.04705	0.047725	1.415212	0.046099	0.046958	1.829398	0.045148	0.046754	3.435154
10	0.050038	0.051742	3.292667	0.048961	0.050751	3.526444	0.047884	0.048272	0.804228
15	0.056958	0.059547	4.348612	0.055615	0.056341	1.288341	0.054272	0.054639	0.670843
Energy (MeV)	S4			S5			S6		
	XCOM	MCNP5	RD (%)	XCOM	MCNP5	RD (%)	XCOM	MCNP5	RD (%)
0.015	94.752	98.59716	3.899867	91.504	94.07678	2.734764	81.32	85.02831	4.361269
0.02	68.781	70.75601	2.791291	65.535	66.92576	2.078065	55.485	57.22402	3.038972
0.03	34.307	35.05805	2.142297	34.851	35.67679	2.314645	36.365	37.20173	2.249161
0.04	16.235	16.54402	1.867847	16.488	17.1196	3.689323	17.19	17.39554	1.18158
0.05	9.041	9.104062	0.692683	9.1739	9.625865	4.695315	9.539	9.940123	4.03539
0.06	5.6113	5.820722	3.597871	5.6885	5.961692	4.582459	5.899	6.10111	3.312676
0.08	2.6638	2.673354	0.35736	2.6943	2.810129	4.121854	2.7755	2.870888	3.322592
0.1	4.5002	4.633479	2.876431	4.3066	4.327718	0.487974	3.707	3.808161	2.656434
0.2	0.81746	0.855792	4.479165	0.78383	0.808126	3.006453	0.6795	0.683088	0.525243
0.3	0.33933	0.348961	2.760045	0.32736	0.334036	1.998514	0.29015	0.292673	0.862073
0.4	0.20137	0.204126	1.349913	0.19554	0.200779	2.609241	0.17735	0.180818	1.917851
0.5	0.14361	0.143974	0.252704	0.14023	0.14398	2.604776	0.12967	0.135181	4.076704
0.6	0.11344	0.114094	0.572952	0.11126	0.112369	0.986544	0.10442	0.105297	0.8325
0.8	0.083078	0.085998	3.395885	0.081974	0.085905	4.576332	0.078495	0.080249	2.185697
1	0.067786	0.070923	4.42315	0.067135	0.070281	4.475695	0.06507	0.065109	0.059909
2	0.044897	0.045764	1.894172	0.044649	0.046073	3.090801	0.043855	0.044821	2.154884
3	0.040972	0.042892	4.476697	0.040698	0.041274	1.394481	0.03983	0.041793	4.697997
4	0.040333	0.040534	0.495538	0.040015	0.040098	0.206792	0.039015	0.040129	2.77552
5	0.040818	0.042456	3.85845	0.040456	0.041646	2.85856	0.039325	0.040486	2.867945
6	0.041768	0.041824	0.134405	0.041364	0.042076	1.691121	0.040105	0.041557	3.494803
8	0.044197	0.045083	1.965589	0.043721	0.045271	3.423985	0.042245	0.04365	3.218653
10	0.046807	0.047748	1.96989	0.046268	0.047765	3.134638	0.0446	0.046373	3.824306
15	0.052929	0.055111	3.959096	0.052257	0.052499	0.461353	0.05018	0.051954	3.415225

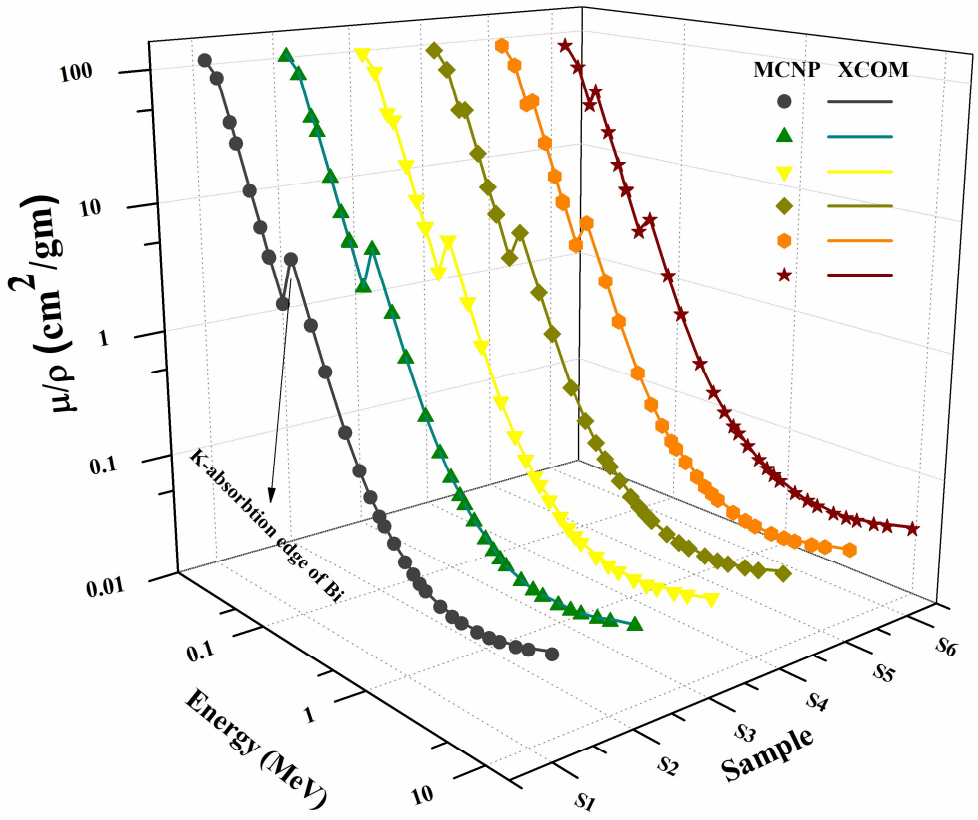

Figure 8. Mass attenuation coefficients (μ_m) computed using the MCNP5 simulation and XCOM software.

The HVL values for the generated alloys were calculated using μ_m values and are presented in Figure 9 as a function of radiation energy. Figure 9 showed that the HVL values for the present alloys are nearly constant for energies below 90 keV, with the highest HVL value seen at 4 MeV. The HVL behavior may be described in a similar mechanism to the previous explanation of μ_m. The results show that the Bi-50Sn alloy has the lowest HVL values, ranging from 0.0005 to 1.579 cm.

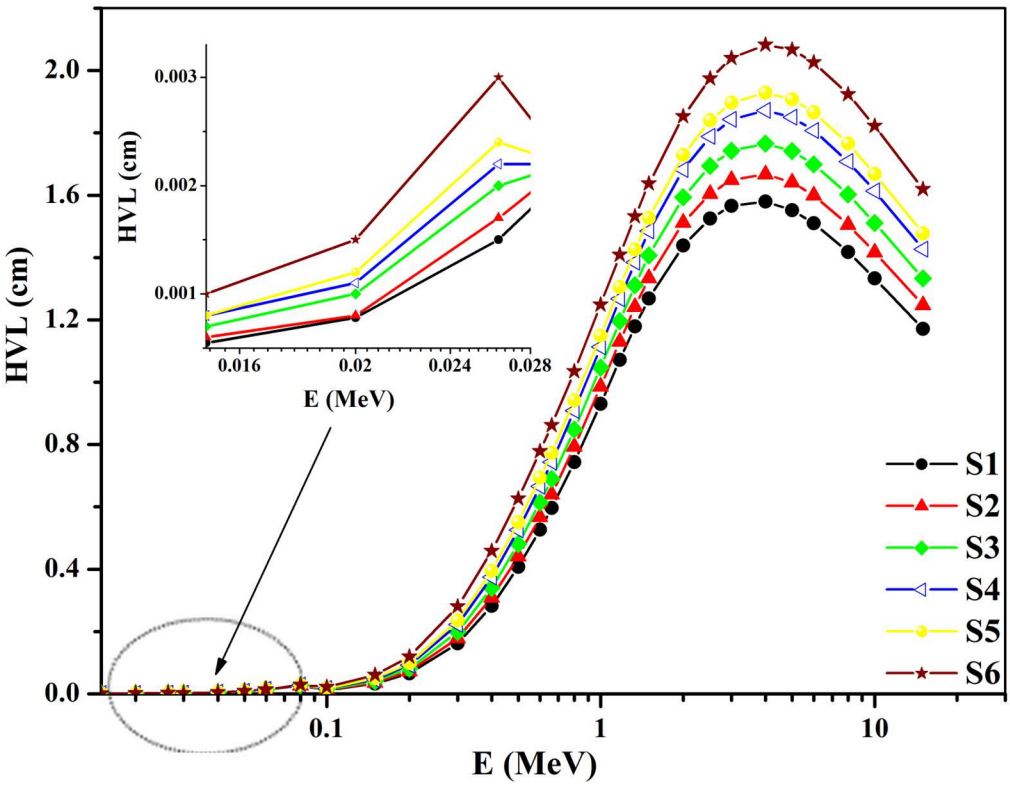

Figure 9. Half value layer (HVL) values of the manufactured samples in terms of radiation energy.

The HVL results obtained for the current alloys were also compared with a number of well-known radiation shielding materials, such as regular concrete, hematite serpentine, basalt magnetite, ilmenite limonite, and a number of recently researched alloys, including Si-B5, Fe-B5, Galinstan, and Cu-Ag0.8, across the available photon energy range [14,25]. According to Figure 10, the Bi-40Pb alloy's HVL is substantially lower than the HVL values of every other prepared sample and of common radiation shielding materials, which validates the use of the current alloys as radiation shielding materials.

The effective atomic number (Z_{eff}) and electron density (N_{el}) of all fabricated alloys exhibited an analogous trend of variation throughout the various photon energy ranges, as seen in Figure 11. With the exception of sample S1, which presented constant behavior through the entire energy range, Z_{eff} and N_{el} levels significantly decreased with increases photon energy up to 0.1 MeV, suggesting that the photoelectric influence predominates in this energy regime.

Due to predominance of the Compton dispersion approach in this energetic lineup, the Z_{eff} and N_{el} values dropped between 0.095 and 1.7 MeV, with the lowest values observed at 30 KeV. Then, between 1.7 up to 15 MeV, both values started to steadily increase as the pair production process became more significant. Importantly, all alloys demonstrated a similar Z_{eff} and N_{el} behavior over the energy domain. This can be attributed to the incorporation of lead (Pb), an element with higher atomic number relative to Sn; this enhances the interaction between gamma rays and Pb atoms, lowering the overall amount of gamma rays that may travel within the alloys. With Z_{eff} and N_{el} values around 82 and 2.34×10^{23}, respectively, the Bi-40Pb sample has the highest values of all manufactured alloys. Materials with higher Z_{eff} values are generally more effective in shielding against gamma rays.

Consequently, from all developed samples, the Bi-40Pb alloy would be a good choice for gamma-ray shielding applications.

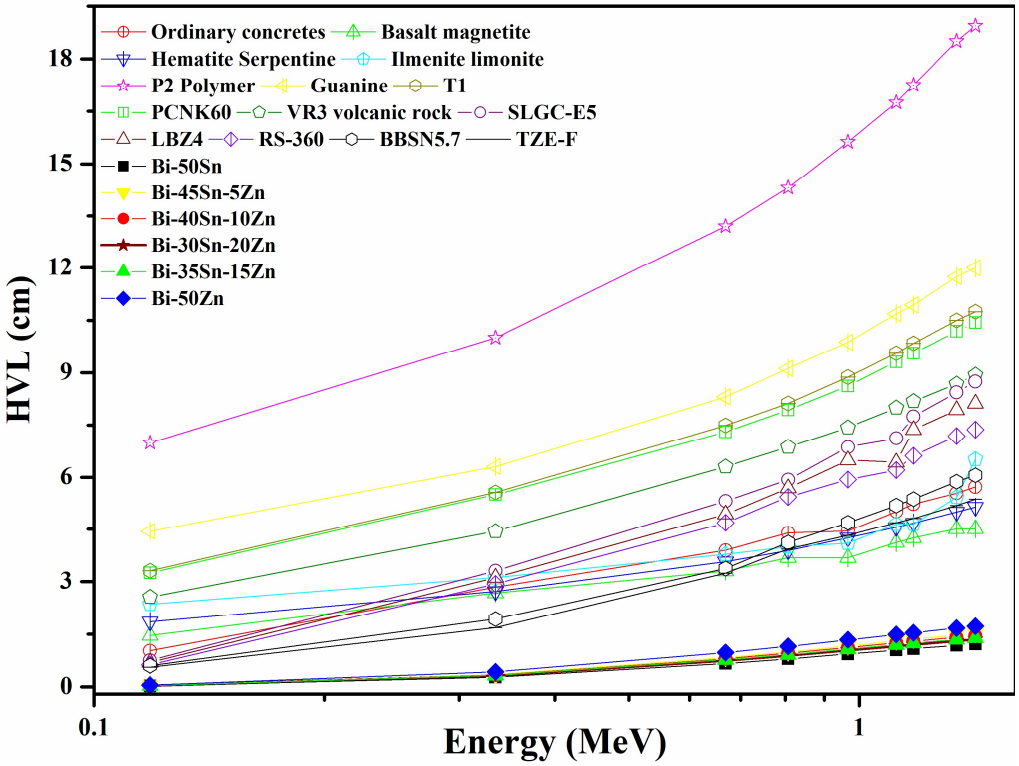

Figure 10. The contrast of the created alloys' HVL values at accessible photon energies with those of certain well-known radiation shielding materials and some materials from recent investigations.

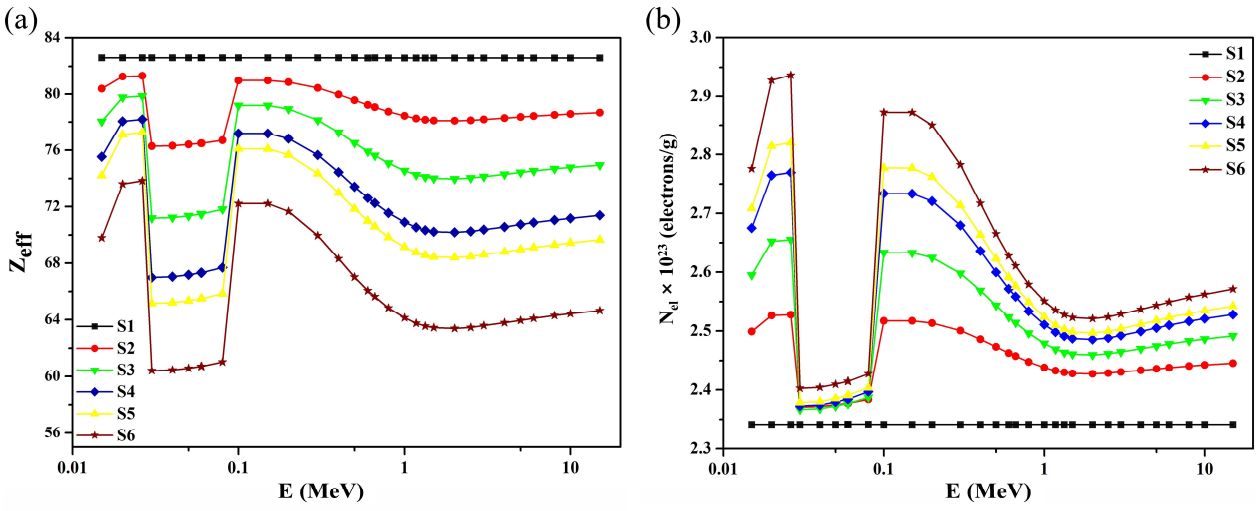

Figure 11. Changes in the generated alloys': (a) Z_{eff} and (b) N_{el} with respect to radiation energy.

Furthermore, using the following formula and accounting for the initial and transmitted photon intensities (I_0 and I), the RPE of the developed alloys can be calculated. The RPE (%) values for these

alloys at a thickness of 2 cm were assessed and are illustrated as a function of photon energy in Figure 12. In can be observed that the RPE of the alloys declines from its peak at 300 keV as photon energy increases. Due to its RPE performance, the Sn-50Bi alloy is recommended for use in X-ray protection, particularly in medical diagnostic applications, as it offers complete (100%) shielding against X-ray exposure at energies above 300 keV. These findings demonstrate that the developed alloys are suitable for use as gamma-ray shielding materials.

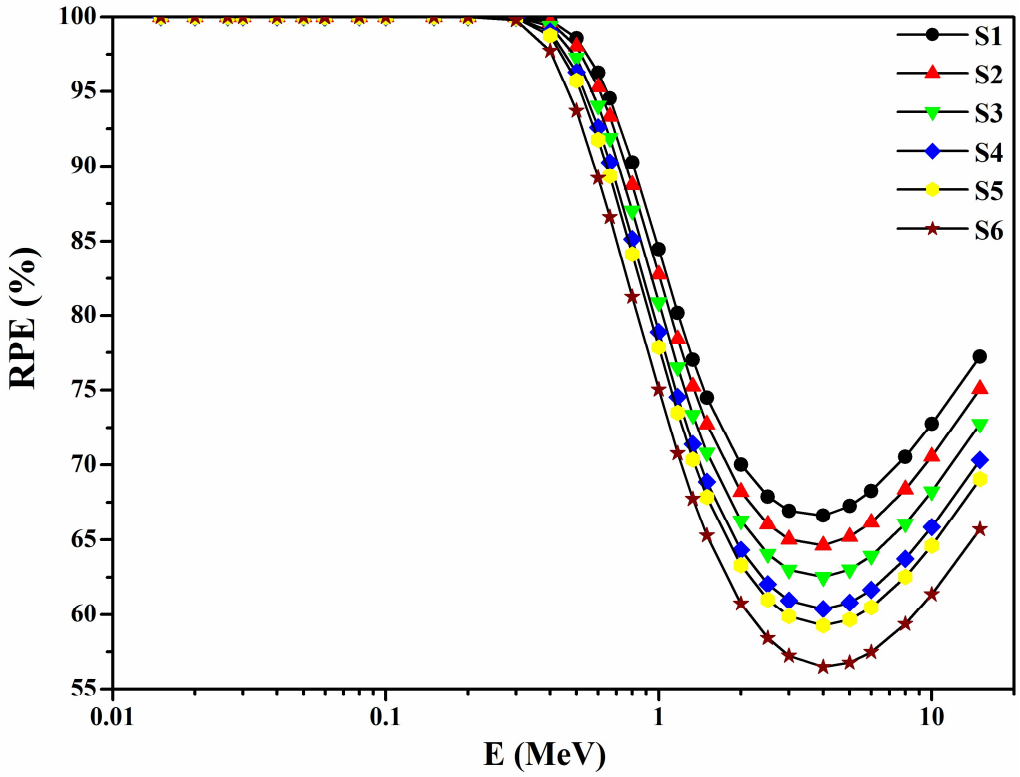

Figure 12. The RPE score (%) of produced alloys in terms of photon energy.

Figure 13 shows the balance between mechanical properties, in terms of Young's modulus (Y_b), and the gamma-ray shielding performance expressed in μm at photon energies of 0.015 and 0.1 MeV. As shown in Figure 13, the Bi-40Pb alloy exhibits the highest shielding efficiency and a moderately high mechanical capability among all alloys. Furthermore, the S5 (Bi-5Pb-35Sn) alloy shows the best mechanical efficiency and reasonably good gamma-ray shielding properties. Overall, the Bi-40Pb alloy shows the highest gamma-ray shielding capability and relatively good mechanical efficiency, making it authorized for use in radiation protection due to its satisfactory balance between mechanical performance and shielding.

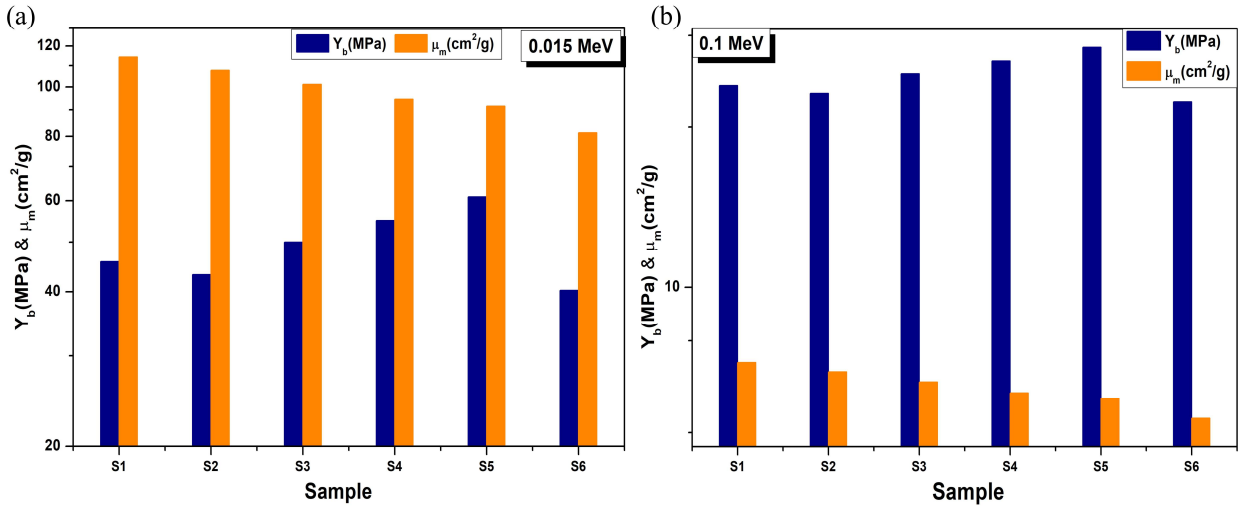

Figure 13. Correlation between mechanical and shielding properties in terms of Y_b and mass attenuation coefficient (μ_m) of the generated alloys at photon energies of (a) 0.015 and (b) 0.1 MeV.

Although Pb significantly enhances both the radiation attenuation and mechanical properties of the studied alloys, its well-documented toxicity and disposal concerns limit its long-term applicability in environmentally sensitive settings. To address this, the current study serves as a stepping stone toward optimized compositions with reduced Pb content. Future work will explore partial or complete substitution of Pb with safer, high-Z elements such as bismuth (Bi), tungsten (W), or tin (Sn), which have demonstrated promising radiation-shielding capabilities while maintaining acceptable mechanical strength.

3.5. Neutron shielding properties

Figure 14 compares $\sum_R$ values for the synthesized alloys with those of well-known neutron shielding materials, including water, graphite, basalt magnetite, and concrete, to evaluate the potential of the current alloys for neutron protection. Among the samples, the S1 alloy (Bi-40Pb) exhibited the highest neutron removal cross-section ($\sum_R$ = 0.1085 cm^{-1}), outperforming the other conventional shielding materials. Consequently, the Bi-40Pb alloy can be considered an excellent candidate for both gamma and neutron radiation shielding applications.

In addition, while neutron attenuation is crucial, the mechanical properties of the alloy should also be considered for practical applications. In this context, the balance between the neutron attenuation properties, in terms of removal neutron coefficient ($\sum_R$), and the mechanical efficacy, in terms of Y_b, of the prepared alloys is illustrated in Figure 15.

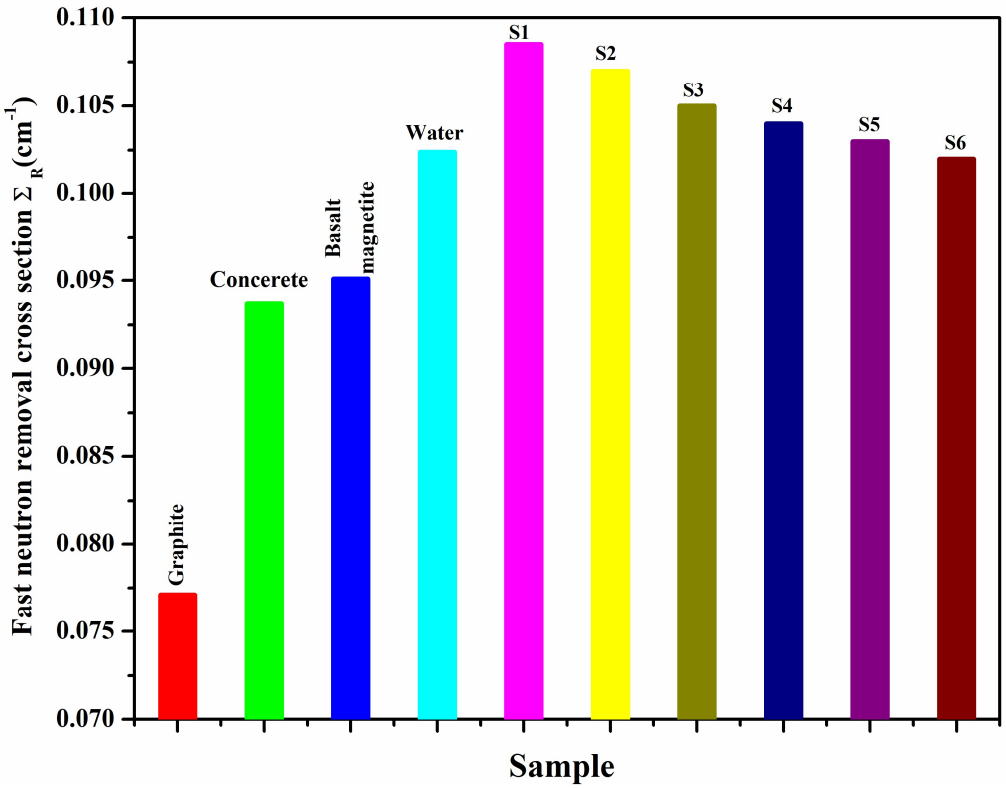

Figure 14. High-energy neutron removal cross-section of the generated alloys in comparison to some of the best neutron attenuation materials.

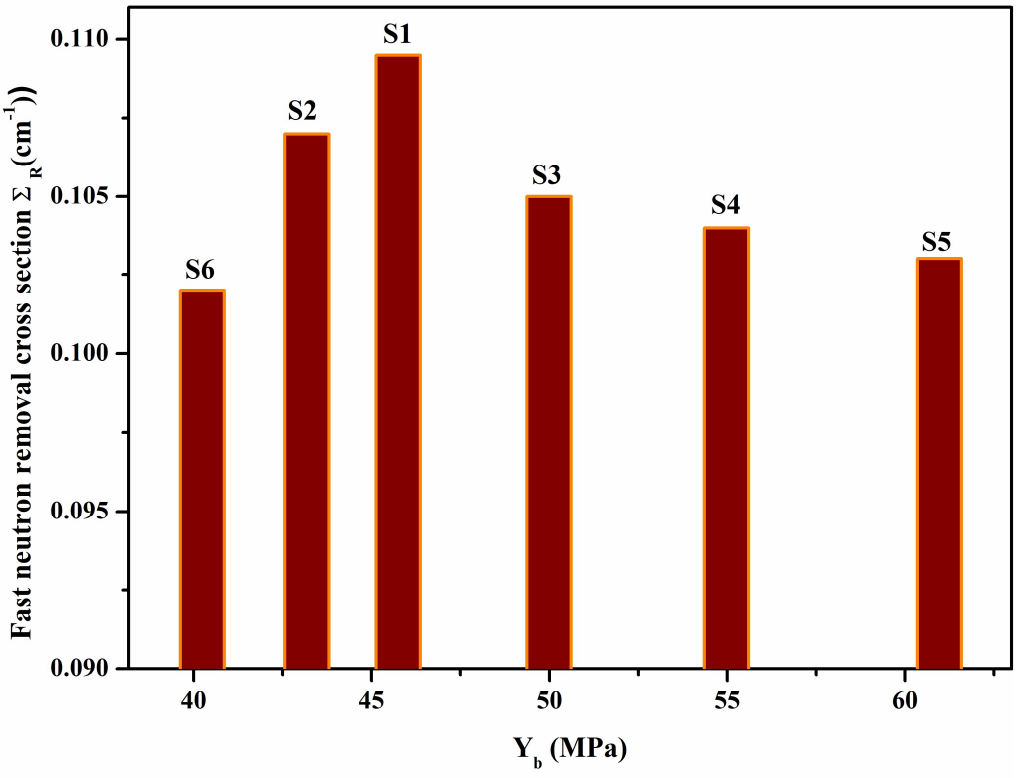

Figure 15. Correlation between mechanical and shielding properties in terms of Y_b and fast neutron removal attenuation coefficient ($\sum_R$) of the generated alloys.

As shown in Figure 15, the Bi-40Pb alloy exhibits the best neutron shielding efficacy and a moderately high mechanical capability among the alloys examined. Furthermore, the S5 (Bi-5Pb-35Sn) alloy has the best mechanical efficiency and reasonably good neutron shielding properties. Nevertheless, the Bi-40Pb alloy presents the highest neutron shielding capabilities because of its relatively good mechanical efficiency, being authorized for use in radiation protection due to its satisfactory balance between mechanical performance and neutron shielding.

4. Conclusions

This study aimed to find a reasonable compromise between the mechanical characteristics and nuclear shielding abilities of six bismuth-based binary and ternary alloys. A number of important implications may be drawn from the results obtained here:

(1) The shill-block melt spinning technique produces materials with notable and unique characteristics, like reduced dimensions of grains and, depending upon the situation, possibly metastable crystalline and amorphous phases, by quickly removing heat effects during the liquid-to-solid state transition.

(2) Physical analysis reveals the production of alloy materials with high density values ranging from 8.53 to 10.39 g/cm^3. The XRD patterns demonstrated the presence of the Bi, Sn, and Pb phases as well as the formation of intermetallic phases, such as Bi0.3Pb0.7 and Sn0.95Bi0.05.

(3) Of all the fabricated alloys, the Bi-5Pb-35Sn alloy had the greatest Young's modulus (60.97 GPa), ductility (7446%), fracture toughness (15.36 MPa m$^{1/2}$), and yield stress (35 MPa), while the Bi-40Pb alloy had comparable values of 45.74 GPa, 3.88%, 5.33 MPa m$^{1/2}$, and 5 MPa, respectively.

(4) The MAC results obtained with the MCNP5 code and XCOM show a high degree of consistency with regard to radiation shielding for all samples. Furthermore, findings show that the S1 sample (Bi-40Pb) offered full shielding against X-ray photons up to 220 keV and might be utilized for X-ray shielding purposes, such as in healthcare diagnosis. Furthermore, at higher gamma-ray energy, this alloy showed somewhat better gamma-ray shielding properties than other alloys that are commonly used as gamma-ray shielding materials.

(5) The Bi-40Pb alloy also had superior neutron shielding properties (0.109 cm^{-1}) in comparison to typical neutron protecting materials, but Bi-50Sn had a comparatively higher $\sum_R$ value.

From a practical standpoint, these findings suggest that the developed Bi-based alloys offer promising radiation shielding materials. Their combined mechanical robustness and radioprotective capabilities make them suitable for applications in medical diagnostic imaging rooms, nuclear facility walls, and transport containers for radioactive materials. Furthermore, the melt-spinning approach offers scalability and uniformity, supporting future industrial fabrication and deployment. These results support the continued development of lead-reduced shielding alloys for safer and more sustainable radiation protection systems.

Use of AI tools declaration

The authors declare they have not used Artificial Intelligence (AI) tools in the creation of this article.

Conflict of interest

The authors declare no conflict of interest.

Acknowledgements

The authors extend their appreciation to the Deanship of Scientific Research at King Khalid University for funding this work through a large group Research Project under grant Number RGP.2/244/46.

Author contributions

Mohamed Saad: data creation, original draft preparation, validation and revision; Nadiah Almohiy: writing, methodology, validation and revision; Hussain AlMohiy: methodology, writing, original draft preparation; Abdelmoneim Saleh: conceptualization, methodology, software, data creation, writing; Rizk Shalaby: writing, original draft preparation, validation and revision.

References

1. Abdelhakim NA, Saleh A, Mitwalli M, et al. (2025) A good balance between the efficiency of ionizing radiation shielding and mechanical performance of various tin-based alloys: Comparative analysis. *Radiat Phys Chem* 226: 112155. https://doi.org/10.1016/j.radphyschem.2024.112155
2. Adib M, Habib N, Bashter I, et al. (2011) Neutron transmission through pyrolytic graphite crystal II. *Ann Nuc Energy* 38: 802–807. http://dx.doi.org/10.1016/j.anucene.2010.11.018
3. Adib M, Habib N, Bashter II, et al. (2013) 2 keV filters of quasi-mono-energetic neutrons. *Yad Fyiz Energ* 15: 419–425. https://doi.org/10.15407/jnpae2014.04.419
4. Adib M, Habib N, Bashter I, et al. (2013) Neutron characteristics of single-crystal magnesium fluoride, *Ann Nuc Energy* 60: 163–171. http://dx.doi.org/10.1016/j.anucene.2013.04.024
5. Sayyed MI, Saleh A, Kumar A, et al. (2024) Experimental examination on physical and radiation shielding features of boro-silicate glasses doped with varying amounts of BaO. *Nucl Eng Technol* 56: 3378–3384. https://doi.org/10.1016/j.net.2024.03.038
6. Adib M, Habib N, Bashter I, et al. (2011) MgO single-crystal as an efficient thermal neutron filter. *Ann Nuc Energy* 38: 2673–2679. http://dx.doi.org/10.1016/j.anucene.2011.08.001
7. Shahboub A, Saleh A, Hassan AK, et al. (2023) EPR studies and radiation shielding properties of silver aluminum phosphate glasses. *Appl Phys A* 129: 410. https://doi.org/10.1007/s00339-023-06681-3
8. Saleh A, Tajudin SM, Algethami M, et al. (2026) Optimizing the integration between radiation protection, optical, and mechanical strength for advanced nuclear safety applications using tungsten-doped bismuth borate glasses. *Radiat Phys Chem* 238: 113216. https://doi.org/10.1016/j.radphyschem.2025.113216
9. Saleh A, Sayyed M, Anjan K, et al. (2024) Synthesis and gamma-ray shielding efficiency of borosilicate glasses doped with zinc oxide: Comparative study. *Silicon* 16: 4427–4435. http://dx.doi.org/10.21203/rs.3.rs-3925330/v1

10. Abd-Elkader OH, Nasrallah M, Nasrallah M, et al. (2024) Rapid fabrication, magnetic, and radiation shielding characteristics of $NiFe_2O_4$ nanoparticles. *Opt Mater Express* 14: 1170–1185. https://doi.org/10.1364/OME.521679
11. Saleh A, Anastasiia K, Basfer N, et al. (2025) Comprehensive examination of synthesis, microstructure, and radiation shielding effectiveness of multi-layered polymeric GNP-nanocomposites. *Rad Phys Chem* 237: 113078. https://doi.org/10.1016/j.radphyschem.2025.113078
12. Agar O, Sayyed MI, Akman F, et al. (2019) An extensive investigation on gamma ray shielding features of Pd/Agbased alloys. *Nucl Eng Technol* 51: 853–859. https://doi.org/10.1016/j.net.2018.12.014
13. Ahmed M, Mohamed M, Abdelghany A (2024) Radiation shielding performance and environmental safety of Bi_2O_3-modified borate glasses. *J Environ Chem Eng* 12: 114693. https://doi.org/10.1016/j.jece.2024.114693
14. Shaban N, El-Kameesy A, El-Mellegy G (2024) Comparative assessment of Bi_2O_3 and barite concretes as lead-free shielding building materials. *Constr Build Mater* 422: 137003. https://doi.org/10.1016/j.conbuildmat.2024.137003
15. El-Khodary A, Abdelmonem M, Yousef A, et al. (2024) Mechanical and radiological characterization of Bi-based glass systems for shielding applications. *J Build Eng* 92: 110496. https://doi.org/10.1016/j.jobe.2024.110496
16. Farag L, El-Desoky M, Abdelghany A (2025) Environmental and shielding performance of Bi_2O_3–BaO–B_2O_3 glasses as Pb-free radiation shielding materials. *Rad Phys Chem* 210: 113015. https://doi.org/10.1016/j.radphyschem.2025.113015
17. Al-Abbas S, Al-Furaiji M, Mebdir H, et al. (2021) Development and characterization of Bi–Sn–Zn ternary alloy for radiation shielding applications. *J Alloys Compd* 861: 158637. https://doi.org/10.1016/j.jallcom.2021.161451
18. Shahid M, Ali A, Khan F, et al. (2018) A comparative study of Bi–Sn and A–Pb alloys for gamma shielding. *J Alloys Compd* 735: 1396–1404. https://doi.org/10.1016/j.jallcom.2018.03.288
19. Ryu H, Lee S, Lim D, et al. (2018) Flexible X-ray shielding material based on bismuth-oxide–epoxy composites for medical imaging applications. *ACS Appl Energy Mater* 1: 976–984. https://doi.org/10.1021/acsaem.8b00179
20. Mostafa A, El-Azab M, Mahmoud S (2017) Structural and gamma ray shielding properties of bismuth oxide-borosilicate glass composites. *J Alloys Compd* 729: 1180–1190. https://doi.org/10.1016/j.jallcom.2017.11.329
21. Mahdy M, Ali M, Al-Ghamdi A, et al. (2024) Effect of Bi_2O_3 addition on optical, structural, and shielding parameters of tellurite glasses. *J Mater Res Technol* 29: 4994–5007. https://doi.org/10.1016/j.jmrt.2024.04.138
22. Chen Y, Wang L, Zhou W, et al. (2025) Preparation of flexible composite with bismuth-based fillers for X-ray and EMI shielding. *Sens Actuators A Phys* 356: 116229. https://doi.org/10.1016/j.sna.2025.116229
23. Chandra S, Ramana B, Gopal V (2023) Structure and radiation attenuation properties of Bi-containing polymer nanocomposites. *RSC Adv* 13: 25031–25044. https://doi.org/10.1039/d3ra04509a

24. Saleh A, Hussain A, Rizk M, et al. (2024) Comprehensive investigation on physical, structural, mechanical and nuclear shielding features against X/gamma-rays, neutron, proton and alpha particles of various binary alloys. *Rad Phys Chem* 216: 111443. https://doi.org/10.1016/j.radphyschem.2023.111443
25. Saleh A, Rizk M, Abdelhakim A (2022) Comprehensive study on structure, mechanical and nuclear shielding properties of lead-free Sn–Zn–Bi alloys as a powerful radiation and neutron shielding material. *Rad Phys Chem* 195: 110065. https://doi.org/10.1016/j.radphyschem.2022.110065.
26. Deghady AM, Tayel A, Saleh A, et al. (2022) Effect of 0.3 wt% TiO_2 nanoparticles on the thermal, structural, and mechanical properties of $Sn_{3.8}Ag_{0.7}Cu_{1.0}Zn$ solder alloy. *Phys Scr* 97: 105709. https://doi.org/10.1088/1402-4896/ac90fb
27. Abdelhakim N, Shalaby R, Kamal M (2018) A study of structure, thermal and mechanical properties of free machining Al-Zn-Sn-Bi alloys rapidly solidified from molten state. *World J Eng Technol* 6: 637–650. https://doi.org/10.4236/wjet.2018.63040
28. Saad, G, Fawzy SA, Fawzy A, et al. (2010) Deformation characteristics of Al-4043 alloy. *Mater Sci Eng A* 527: 904–910. https://doi.org/10.1016/j.msea.2009.09.018
29. Abdelmonem AM, Soliman M, Saleh A (2026) Investigation of some radiation protection properties of borate glasses system doped with different percentages of PbO. *Radiat Phys Chem* 239: 113396. https://doi.org/10.1016/j.radphyschem.2025.113396
30. Alshihri AA, Saad M, Almohiy H, et al. (2026) Comparative study of improving the mechanical, structural, and simulated ionized radiation shielding properties of bismuth-reinforced tin-based alloys. *Radiat Phys Chem* 240: 113405. https://doi.org/10.1016/j.radphyschem.2025.113405
31. Alharbiy N, Khattari ZY, Rammah YS, et al. (2023) Role of Al_2O_3, WO_3, Nb_2O_5, and PbO on the physical, elasto-mechanical and radiation attenuation performance of borotellurite glasses. *J Mater Sci Mater Electron* 34: 191. https://doi.org/10.1007/s10854-022-09604-9
32. Shahboub A, El Damrawi G, Saleh A (2021) A new focus on the role of iron oxide in enhancing the structure and shielding properties of Ag_2O–P_2O_5 glasses *Eur Phys J Plus* 136: 947. https://doi.org/10.1140/epjp/s13360-021-01948-1
33. Li Z, Chen L, Chang F, et al. (2022) Synthesis, microstructure and properties of Ti(C,N)-(HfZrTaNbTi)C_5-HEA high-entropy cermets by high-energy ball milling and spark plasma sintering. *Ceram Int* 48: 30826–30837. https://doi.org/10.1016/j.ceramint.2022.07.036
34. Kavak S, Bayrak KG, Bellek M, et al. (2022) Synthesis and characterization of (HfMoTiWZr)C high entropy carbide ceramics. *Ceram Int* 48: 7695–7705. https://doi.org/10.1016/j.ceramint.2021.11.317
35. Peyrouzet F, Hachet D, Soulas R, et al. (2020) Correction to: Selective laser melting of $Al_{0.3}$CoCrFeNi high entropy alloy: Printability, microstructure, and mechanical properties. *JOM* 72: 3705. https://doi.org/10.1007/s11837-020-04149-w